A Continuum Model of Deformation and Damage for API X70 Steel Based on the Theory of Strain Gradient

Mohammed Anazi and Hussein Zbib
Washington State University
School of Mechanical and Materials Engineering

Abstract

This work shows the results of a continuum model of deformation and damage for API X70 steel based on the strain gradient theory. The model is developed according to the continuum mechanics of the elastic/viscoplastic framework. The constitutive equations of the model include the dislocation theory according to the roles of the statistically stored and geometrically necessary stored dislocation densities during plastic deformation. In addition, effects of nucleation and growth of voids are considered within the constitutive equations as a ductile failure based on a classical isotropic damage model. Then, the model is examined for scale and strain rate effects. The developed model is implemented into LS-DYNA® by writing a subroutine within USER_DEFINED_MATERIAL_MODELS (UMAT). A ASTM tensile test is simulated to examine the validity of the model. The results show a good agreement with experimental data found in the literature.

Introduction

API X70 is high strength low alloy steel that is used in manufacturing pipelines for crude oil and natural gas transportation worldwide. It is a member of API steel family that is standardized by American Petroleum Institute (API) and ranges from X47 to X120 grade [1]. The number after the X denotes the yield strength in ksi. Each grade has different chemical properties and thermomechanical fabrication processes that determine its mechanical properties such as strength, toughness, and ductility deformation or ductile failure. One of the most effective ways to evaluate the strength and deformation of a material is by utilizing a tension test. The strength and deformation of X70 has been investigated in many studies over the last two decades[2–18]. The investigations are still being performed on X70 to guarantee its long-life service under high operational pressure.

In addition to the experimental works are performed on X70, there are several numerical attempts to describe its strength and deformation behavior based on classical continuum deformation theories. In the classical deformation theories, the stress is related to the strain in a straightforward way. Thus, a short literature review presents the models that have been used thus far to describe the deformation and the ductile failure of X70. De Luna et al. structured a continuum model for analyzing the static and dynamic fracture behavior of X70 [19]. The model they introduced was based on a power law that describes the plastic deformation, but the ductile failure was described by Rice and Tracey model [20]. In addition, Rivalin et al. established a continuum model based on Norton's law [21] for the viscoplastic behavior and a simple power law for the hardening behavior, and they used the Gurson-Tvergaard-Needleman (GTN) continuum damage model [22] for softening or ductile failure in order to simulate in-plane crack propagation in wide plates of X70 [4]. However, Chen et al. analyzed the ductile tearing of X70 in single edge notch tension specimens [9]. In the analysis, Ramberg-Osgood power-law [23] described the plastic flow behavior, while the GTN model was used for describing the softening behavior. With the same model, Chen et al. simulated the numerically ductile tearing in X70 wide plates for semi-elliptical surface cracks [5]. Then, Kim et al. compared a simulation of a ductile failure of X70 with an experiment by using a phenomenological stress-modified fracture strain model [24] [8]. Lastly, Paredes et al. [13] modeled X70 based on the J_2 theory of plasticity. Here, a simple hardening law was used. Their work focused on the post necking stage for predicting a crack initiation and propagation. However, for softening, Paredes et al. used the model that was introduced by Li and Wierzbicki [25] which is based on a non-linear power law.

Paredes et al. modeled the fracture initiation and propagation based on the modified Mohr-Coulomb fracture criterion [26]. These studies that have been conducted to describe the deformation and ductile failure of X70 numerically.

After surveying the relevant literature, the previous models are based on the conventional continuum theories that do not consider the internal material variables, such as dislocation density. Literature Models of the deformation and ductile failure of X70 lack a model that employs the dislocation density theory, despite the dislocation density being responsible for the aspects of materials deformation. During fracture, for example, the interactions of dislocations and voids determine whether a behaviors of a cleavage is brittle or ductile by influencing the stress field near the crack tip [27,28]. In addition, the tearing failure is a common problem that X70 pipelines encounter. Therefore, a deformation model based on the strain gradient theory is developed in this research to study X70 deformation.

The strain gradient theory is approached in different ways. First, it is approached by taking the gradient of the of plastic shear strain to address the density of geometrical necessary stored dislocations in order to homogenize the heterogeneity of alloy deformation and accommodate the curvature change during deformation [29]. In addition, the strain gradient theory estimates the size dependent phenomena of the plastic deformation behavior in sub-micro scale problems that classical plasticity theories lack [30]. Here, the gradient of the plastic shear strain is implicitly imbedded in the hardening equations [31]. Another approach of the strain gradient is to study and describe the softening behavior of materials [32,33]. Also, it is used to solve the instability of the finite element method during the softening behavior. Here, the gradient of plastic shear strain is used explicitly in plastic flow equations [34]. In addition to these approaches, the higher order gradient (Laplacian) [35] is used. Since the scope of this research does not focus on the strain gradient theory, these cited works give an adequate idea about the theory. Thus, the first approach of the strain gradient theory is used in this work to consider dislocation density during the deformation. More elaboration is provided in the constitutive equations section.

X70 steel experiences a ductile failure or softening that directs our model to adopt a ductile failure criterion. According to the continuum damage theory, the ductile failure is ascribed to voids nucleation, growth, and coalescence processes at micro scale during plastic deformation [28,36–39]. There are several continuum damage models such as the continuum damage mechanism (CDM) [40,41], the GTN [22,42], the Rousselier model [43], the Rice and Tracey model [20], and the Perzyna model [44]. The Perzyna model is used in this work because it fits directly into the deformation model without needing for a vital modification to the constitutive equations. Moreover, the Perzyna model has few variables that must be determined during the simulations. Perzyna established an elastic/viscoplastic model that interprets the postcritical behavior and fracture of dissipative solid by considering the void volume fraction as a parameter that measures internal imperfections [44]. The ductile failure or fracture is a consequence of nucleation, growth, and linkage of voids due to the plastic deformation and stress state that exceeds the yield stress point. Perzyna also postulated that the volume fraction parameters are equivalent to nucleation, growth, and transport or diffusion parameters of voids, but he dropped the transport component because it is only significant at an elevated temperature. Thus, the model is reduced to a simple form of nucleation and growth of voids.

This work implements constitutive equations based on the strain gradient theory in a LS-DYNA UMAT subroutine to describe the plastic deformation of X70. Also, the Perzyna model for void nucleation and growth is implemented to describe the ductile failure or softening. Then, a tension test is simulated at different strains and mesh sizes, and the results are then compared to the experimental results. The experimental work that is used for comparison is the work done by Wang et al. [16].

Constitutive equations

Since the UMAT subroutine requires a user to use the strain as the input to the constitutive equations and update the state of stress, the equations are formulated and proceeds according to the using of the subroutine [45]. A boldface font is used for tensors. As mentioned earlier, X70 is modeled based on the elastic/viscoplastic framework. Therefore, the constitutive equations of the model are based on the assumption that the total strain rate tensor $\boldsymbol{D}$ $(= \boldsymbol{D}^e + \boldsymbol{D}^p)$ can be additively decomposed into an elastic part $\boldsymbol{D}^e$ and plastic part $\boldsymbol{D}^p$**.** For the elastic strain rate, the material obeys the general Hook's law of linear isotropic elasticity based on the formation introduced by Navier and Lame [46], but the formulation is modified to consider the total damage parameter, ξ, i.e.,

$$\dot{\boldsymbol{\sigma}} = ((\lambda\, tr\boldsymbol{D}^e)\mathbf{I} + 2\mu\boldsymbol{D}^e)\left(1 - \sqrt{\xi}\right), \tag{1}$$

where $\dot{\boldsymbol{\sigma}}$ is the Cauchy stress rate tensor, $\mathbf{I}$ is the unit tensor, and λ and μ represent Lame's elastic constants. Then, the equation for plastic deformation is formed, while bearing in mind that X70 is an incompressible isotropic solid. Consequently, the plastic deformation is dependent on the Cauchy deviatoric stress, as follows:

$$\boldsymbol{\sigma}' = \boldsymbol{\sigma} - \frac{\boldsymbol{tr(\sigma)}}{\mathbf{3}}\mathbf{I} \text{ or } \boldsymbol{\sigma}' = \boldsymbol{\sigma} - \sigma_M\mathbf{I}, \tag{2}$$

and σ_M represents the mean normal stress. Next, the model is formed based on an elastic/viscoplastic framework; thus, there is a time dependent behavior for X70 during plastic deformation. Consequently, the model does not involve yield condition, while the transition between elastic and plastic deformation is controlled by a simple power law [47] that shows different yield values at different strain rates as required by the viscoplastic theory [48]. Before stating the power law, the power law is a scalar, while the previously mentioned stress state is a tensor. Therefore, the invariant function of stress is used in this case. The effective stress is based on the von Mises formulation that can accommodate the isotropic behavior of X70. Also, softening is implemented into the model, making the plastic flow dependent on the deviator stress and first invariant of stress, I_σ :

$$\phi = \sqrt{\frac{1}{2}\boldsymbol{\sigma}' : \boldsymbol{\sigma}'} + \alpha_d\, I_\sigma, \tag{3}$$

where $\alpha_d = \beta\xi$. Generally, β is a material parameter, and it determines how much influence ξ has on the flow stress. Then, the plastic flow is assumed to follow the normality rule that is based on the plastic potential Eq. (3), so the plastic strain tensor is formulated as follows:

$$\boldsymbol{D^p} = \dot{\bar{\gamma}}^P \frac{\boldsymbol{\partial\phi}}{\boldsymbol{\partial\sigma}} = \dot{\bar{\gamma}}^P \boldsymbol{M_s'}, \tag{4}$$

where the orientation tensor $\boldsymbol{M_s'} = \boldsymbol{M_s} + \alpha_d\mathbf{I}$, $\boldsymbol{M_s} = \boldsymbol{\sigma}'/2\sqrt{\boldsymbol{\sigma}' : \boldsymbol{\sigma}'/2}$.

Theoretically, softening also influences the hardening of the material, therefore it is incorporated into the power law denominator that is responsible of the hardening. Thus, the power law becomes as follows:

$$\dot{\bar{\gamma}}^P = \dot{\gamma}_0 \left(\frac{\bar{\tau}}{\tau^*\left(1-\sqrt{\xi}\right)}\right)^{\frac{1}{m}}. \tag{5}$$

where $\dot{\bar{\gamma}}^P = \sqrt{2\boldsymbol{D}^p : \boldsymbol{D}^p}$ is the effective or equivalent plastic shear strain rate, $\bar{\tau} = \boldsymbol{\sigma} : \boldsymbol{M}'_{\boldsymbol{s}}$, the effective shear stress, $\dot{\gamma}_0$ a material constant that is about 0.001 s^{-2}, m strain rate sensitivity, and τ^* represents the work hardening component. Hardening is formulated according to the modified Taylor hardening formula [49] to describe the work hardening based on the dislocation density:

$$\tau^* = \tau_0 + \alpha\mu b\sqrt{\rho_t}, \tag{6}$$

where τ_0 represents the yield shear stress, α represents a material constant that varies from 0.3 to 0.5, and b represents the burgers vector magnitude. Here, ρ_t represents the total of the dislocation density that introduces the dislocation density theory to the model. ρ_t is an internal state variable that determines the work hardening of the overall plastic deformation behavior. The work hardening occurs because of the interactions of dislocations [27]. More dislocation density means more interactions that requires more load to be applied to deform a material further.

To describe this phenomenon numerically, ρ_t must be explained further. ρ_t is an aggregation density of preexisting dislocations, ρ_0, statistically stored dislocations, ρ_{ss}, and geometrically necessary stored dislocations, ρ_{GND}. According to the strain gradient theory, ρ_{ss} is the predominant factor in contributing to the work hardening at macroscale problems. It is determined according to the following formulation [29]:

$$\dot{\rho}_{ss} = \alpha_4 \frac{\dot{\bar{\gamma}}^P}{b\bar{\lambda}}, \tag{7}$$

where α_4 represents a constant of order of unity, and $\bar{\lambda}$ represents the mean free path that is the average of a distance traveled by a line of dislocation before being halted by another line of dislocation or an obstacle. it is determined to be $\bar{\lambda} = \frac{1}{\sqrt{\rho_t}}$, and it is on the order of a few nanometers.

The geometrically necessary dislocation density ρ_{GND} plays a significant role at sub-micron scale [31,50,51]. By considering ρ_{GND}, the strain gradient is considered; therefore, the size effect is also considered [52]. It is formulated based on the equivalent plastic shear strain gradient as follows:

$$\rho_{GND} = \frac{\|\nabla\bar{\gamma}^P\|}{l}, \tag{8}$$

where l represents the characteristic length that is about $10^4 b$ [51].

The evolution of the total damage parameter or voids parameter ξ is assumed to consist of two parts, the nucleation part ξ_N and the growth part ξ_G, as follows [44]:

$$\dot{\xi} = \dot{\xi}_N + \dot{\xi}_G \,, \tag{9}$$

where the growth of voids is defined by the following evolution equation [44]:

$$\dot{\xi}_G = (1 - \xi)\eta(tr\boldsymbol{D}^{\boldsymbol{p}}) \,, \tag{10}$$

where η is taken as a constant in the Perzyna model [44]. However, η has been assumed to be a function to describe the voids growth by Pilling et al. [53]. Then, it was modified by Khaleel et al. [54] to become a function in $\bar{\sigma}$, σ_M, m, and Ξ, which is a material constant that is independent of temperature and strain rate. Thus, in this work, η is assumed to be based on the modification by Khaleel et al. [170]:

$$\eta = \Xi \frac{3}{2}\left(\frac{m+1}{m}\right)\sinh\left[2\left(\frac{2-m}{2+m}\right)\frac{\sigma_M}{\bar{\sigma}}\right]. \tag{11}$$

Then, the nucleation of the voids is formulated by the following equation:

$$\dot{\xi}_N = F(\bar{D}^{p^z})\frac{\boldsymbol{\sigma}:\boldsymbol{D}^p}{(1-\xi)}, \tag{12}$$

where F represents a material constant that is independent of temperature and strain rate, $\bar{D}^p$ is the effective plastic strain, and z represents a material constant.

Numerical implementation

The constitutive equations are implemented in a LS-DYNA UMAT subroutine. LS-DYNA is a commercial finite element analysis solver that is favorable for solving high strain rate problems such as explosions and collisions. LS-DYNA solver uses a dynamic code of finite element analysis that seeks dynamic equilibrium for Cauchy's equations of motion [46,55]. However, LS-DYNA can be switched into a static equilibrium where the acceleration is not considered. The UMAT subroutine is a window allows users to implement a model for particular applications.

Numerical simulations of a tensile test according to ASTM standards are conducted, and the tensile test specimen is modeled according to the sub-size specimen dimensions [56]. The grip sections are eliminated to reduce the computational time. In Table 1, the parameters are imported from the work that is done by Wang et al. [16] except for the damage parameters that are curve fitted. Flow curves of the simulations are compared with the experimental result of X70 that was reported by Wang et al. [16]. In addition, true and engineering flow curves are used as a benchmark for the curve fitting process. Then, the curve fitting process is conducted to fit the simulations results with the experimental results, and the process is conducted over two stages: no damage and damage stages. During this process, the α_4, ρ_0, β, Ξ, and F parameters were curve fitted to make the simulations agree with the experiment work.

The parameter α_4 is an internal material constant that specifies at which rate is ρ_{ss} evolves to provide the right work hardening. Then, ρ_0 is curve fitted for a refined fit of curves. Next, the last three parameters are damage parameters that are curve fitted to experiment curves because they were reported for a superplastic material by Khaleel et al. [54]. In addition, the z value is not changed from what was reported in the work by Khaleel et al. [54]. However, m is determined to be 0.0134 based on the work by Wang et al. where he reported flow curves at different strain rates. Flow curves of strain rates, 0.01 s^{-1} and 0.001 s^{-1}, are used to determine m. Table 1 shows the parameters for the simulations after the curve fitting process is conducted.

The model is examined at different strain rates and sizes. However, this research uses 0.001 s^{-1} for the main analyses of the study. For size-effect examination, the specimen is downscaled to nanoscale dimensions, while keeping all the specimen aspects same. Also, the same macroscale parameters are assumed for the nanoscale. Along with all the analyses, the mesh sensitivity is considered. Therefore, the simulations are performed over to mesh sizes, 756 and 6048 elements. Finally, α_4 and β are mesh size dependent as is shown in the results and discussion section.

Table 1: *X70 parameters for the constitutive equations.*

Density	**Young's modulus**	**Poisson ratio**	**Yield shear stress**	**An empirical constant in Taylor hardening law**	**Burger vector**
ρ (kg/m^3)	E (GPa)	ν	τ_0 (GPa)	α	b (m)
7800.0	210.0	0.3	0.327	0.3	$2.5\cdot10^{-10}$
Shear strain rate hardening	**Strain rate sensitivity**	**Initial dislocation density**	**Bulk modulus**	**Numerical constant of order of unity**	**Shear modulus**
γ_0(s^{-1})	m	ρ_0 (m^{-2})	K (GPa)	α_4	μ (GPa)
0.001	0.0134	$1\cdot10^{12}$	175.0	0.08	80.7
Lame' constant		**Damage Parameters**			
λ (GPa)		β	Ξ	F	z
121.0		1.75	0.01	0.004	2.0

Results and Discussion

To validate the model results, the simulations are conducted over two stages, no damage and with damage. First, tension test simulations without a damage criterion $\xi = 0$ are conducted to generate true flow curves and then compared to the experiment curve, as shown in Figure 1. The strain in the figures is up to 0.02 because the true flow curve of the source experiment was reported up to this point. Then, α_4 and ρ_0 are studied to have a well agreement between the simulation and experiment. By studying these parameters, α_4 controls the hardening of the material during plastic deformation, while ρ_0 controls the initial yield point of the curve from a simulation perspective. This behavior can be explained from physical perspective that α_4 is responsible for the evolving rate of ρ_{ss} determining the hardening of materials. More dislocations create more resistance for the plastic flow, in order to overcome this issue, more applied load is needed to create further deformation. This explanation is according to the dislocation theory by the pioneer work of Taylor [49][27]. ρ_0 represents the preexisting dislocation density that is a part of the yield strength. Lowering ρ_0 to 10^7 m^{-2} provides a simulation that shows a good agreement with the experiment result, but this is an unrealistic value that means X70 has nearly a perfect crystalline structure. From a simulation perspective, this value shows that the model does not need to consider the preexisting dislocation density to run a simulation because ρ_{ss} evolves adequately. Figure 2 shows ρ_{ss} versus true strain for ρ_0 at 10^7 m^{-2} and 10^{12} m^{-2}. In general, the model shows a good agreement with experiment without damage, as shown in Figure 1 B.

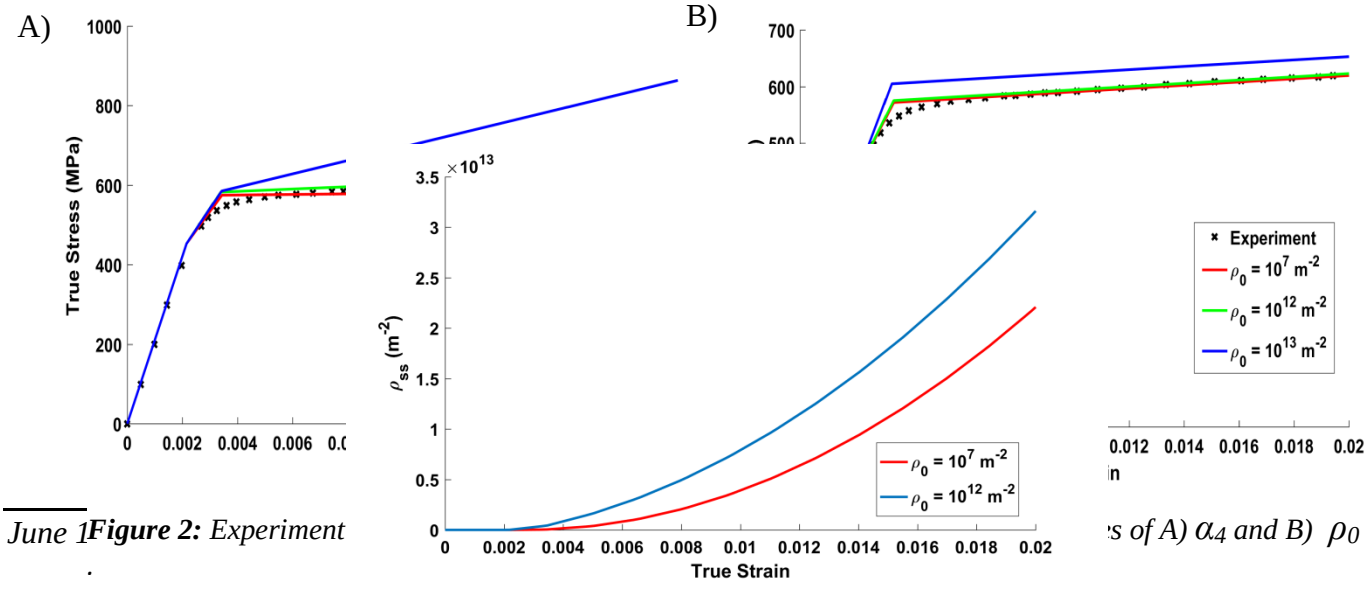

Figure 1: *The evolution of ρ_{ss} at different values of ρ_0 .*

Then, the time of the simulations is extended to obtain large strain to determine if any geometrical instability occurs for the model. The model shows homogenized deformation throughout the gauge length of the specimen, as shown in Figure 3. In addition, a snapshot of the stress contour at the end of the simulation does not show localization. A plateau of the curve occurs at large strain with large stress that are behind the capability of X70. Therefore, the model does not show any strain localization.

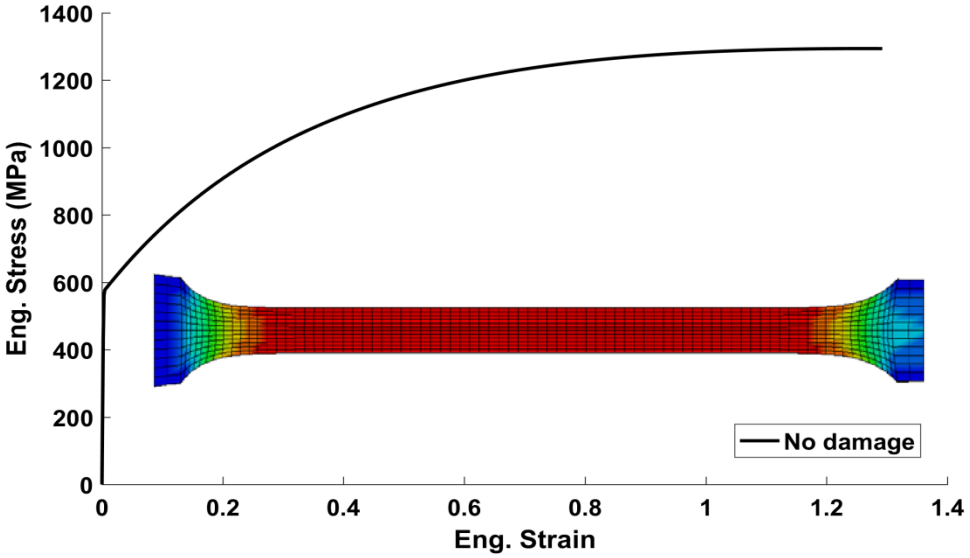

Figure 3: *Simulation without damage criterion at a large strain that is more than 1.0.*

A mesh size analysis was performed at two different mesh sizes, 756 and 6048 elements. the model shows no mesh size sensitivity. The simulations are stopped at the maximum experiment strain that is 0.23, as shown in Figure 4. Although the gradient of plastic shear strain has no effect on the mesh size because ρ_{GND} is insignificant compared to ρ_{ss} when the model is simulated at the macroscale. Figure 5 shows the accumulated ρ_{ss} and ρ_{GND} versus $\bar{\gamma}_p$ and snapshots of the contours of ρ_{ss} and ρ_{GND} at the end of the simulation. The contour of ρ_{ss} spreads all over the gauge length, while the contour of ρ_{GND} presents the maximum ρ_{GND} values are at the opposite corners of the gauge length. The main contribution of work hardening comes from ρ_{ss}. Thus, ρ_{GND} can be ignored if the model is used for a macroscale problem [52].

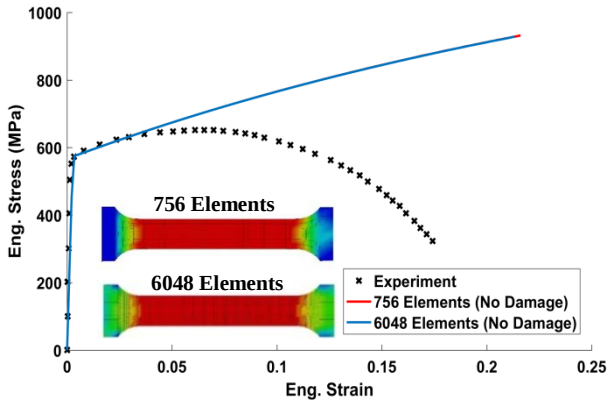

Figure 4: *Mesh sensitivity for the undamaged model.*

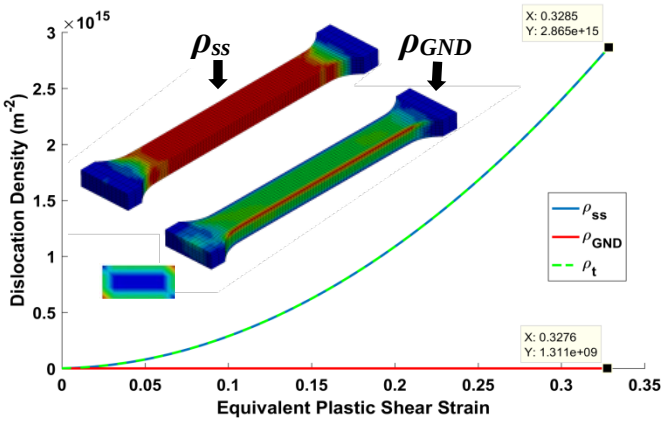

Figure 5: *Accumulation ρ_t, ρ_{ss}, ρ_{GND} and dislocation densities.*

To examine the size effect of the model, the nanoscale specimen is simulated by assuming X70 has the same parameters of the macroscale. In this case, the specimen is just downscaled to nanoscale dimensions while keeping the other aspects of the specimen same. As a result, ρ_{GND} has a significant contribution for the work hardening at nanoscale, as shown in Figure 6. The red solid curve shows ρ_{GND} for the nanoscale specimen, while the dash red curve shows ρ_{GND} for the macroscale specimen, but the blue curves represent ρ_{ss} for both cases. The size effect of the model increases the strength at the nanoscale specimen, as shown in Figure 7. The snapshot of the stress contour for the nanoscale specimen shows a large amount of stress at the opposite corners of gauge length of the specimen and portion of the specimen; this is attributed to ρ_{GND} where it is as significant as ρ_{ss} at a nanoscale case. This finding aligns perfectly with the strain gradient theory. Furthermore, the mesh size shows an effect on the numerical solution at the nanoscale case, because ρ_{GND} is a mesh dependent quantity since it dependent on the plastic shear strain gradient. Figure 8 shows mesh dependence of the model at nanoscale and compares the nanoscale results to the macroscale results. Thus, the model shows slight mesh sensitivity at nanoscale and capturing the size effect when ξ = 0.

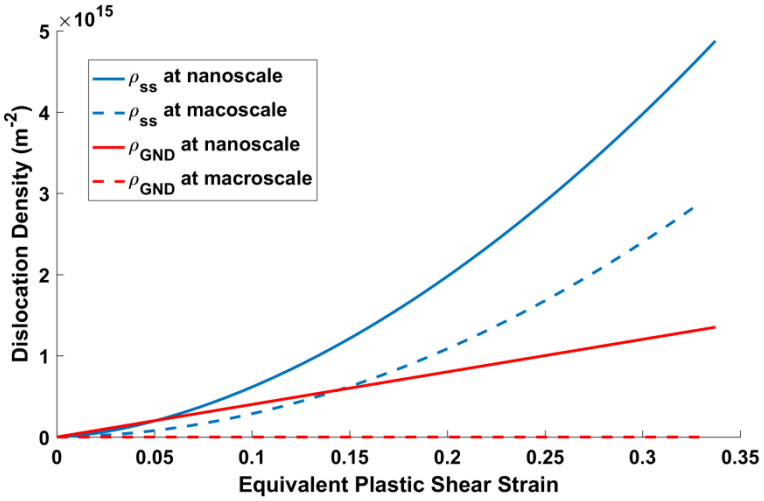

Figure 8: *Dislocation densities comparison between macroscale and nanoscale specimens.*

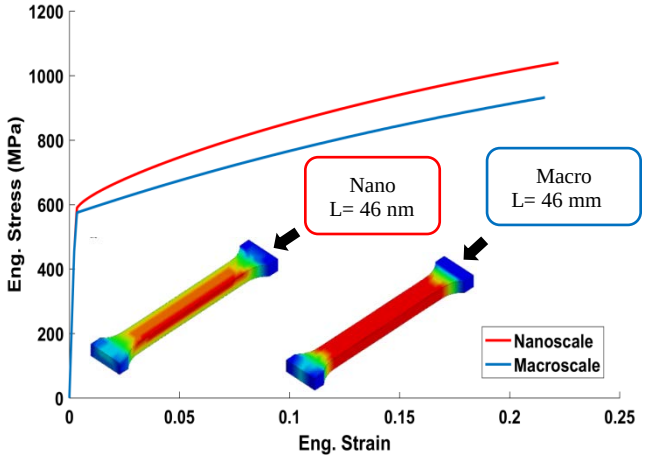

Figure 7: *Flow curves comparison between macroscale and nanoscale specimens. The snapshot is for stress contour. L is the total length of the specimen.*

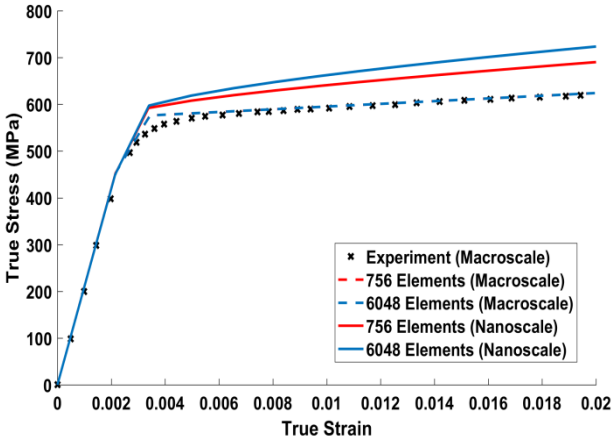

Figure 6: *Mesh sensitivity of the nanoscale model and compared with the macroscale model.*

In the second stage, the model is simulated with the damage criterion, where $\xi \neq 0$. The curve fit process is conducted to determine the parameters of the damage model. The results indicate that the model shows more sensitivity to β than other damage parameters. In Figure 9, all other damage parameters are kept fixed, as stated in Table 1, but β is controlled to provide the best fit with the experiment. Next, the model was examined at different strain rates, as shown in Figure 10, and the model shows good agreement with the experiment result.

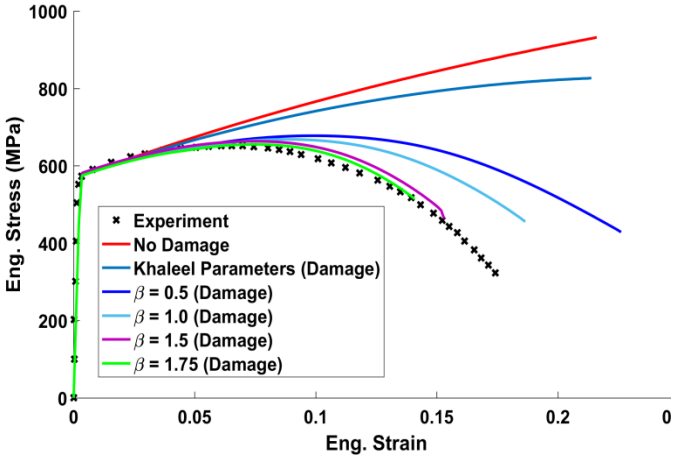

Figure 9: *The curve fitting process by controlling β.*

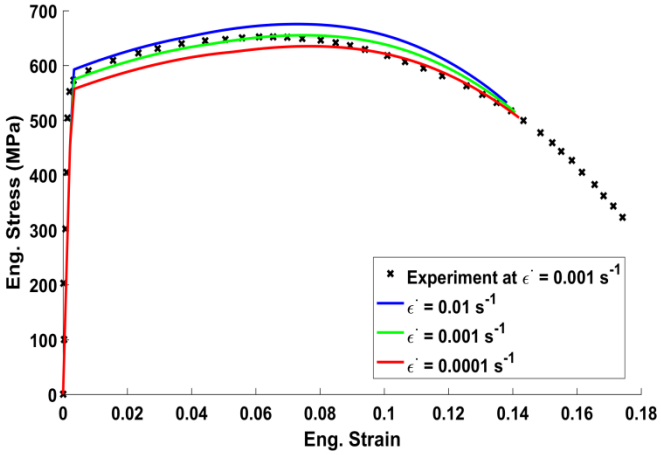

Figure 10: *The damaged model at different strain rates and compared with the experiment result at a strain rate of 0.001 s^{-1}.*

Next, mesh sensitivity analysis is conducted on the model, and the model shows extreme dependency upon the mesh size. To curve fit the simulation to the experiment at different mesh sizes, only the mesh sensitive parameters, α_4 and β, are calibrated, as shown in Figure 11. At 756 elements mesh, the best fit was obtained when α_4 is 0.08 and β is 1.75, as stated in Table 1. However, when 6048 elements mesh is used for best fit, α_4 and β are 0.12 and 0.1, respectively. Also, 6048 mesh is more numerically stable than 756 mesh. It reached $\xi \approx 0.65$ before it became numerically unstable. To validate the use of these parameters and to insure that the model generates reasonable values, the two meshes values of ρ_t and ξ are compared, as shown in Figure 12 and Figure 13. In this comparison, the simulation runs up to the maximum strain of 756 mesh, before it is stopped. ρ_t corresponds to a value within ρ_t range found in literature. For example, ρ_t has been estimated experimentally to be between 3.0×10^{15} m^{-2} and 6.0×10^{15} m^{-2} for similar kinds of steel [57–59]. Also, the results of ξ are reasonable for both meshes. However, the snapshot of ξ contour are presented as bands at about 45° with respect to the load direction, as shown in Figure 13. However, since the model results show homogenized deformation and no localization, the bands are manifolded across the gauge length as the mesh is refined. Thus, the curve fitting process to generate well fit simulation curves is valid.

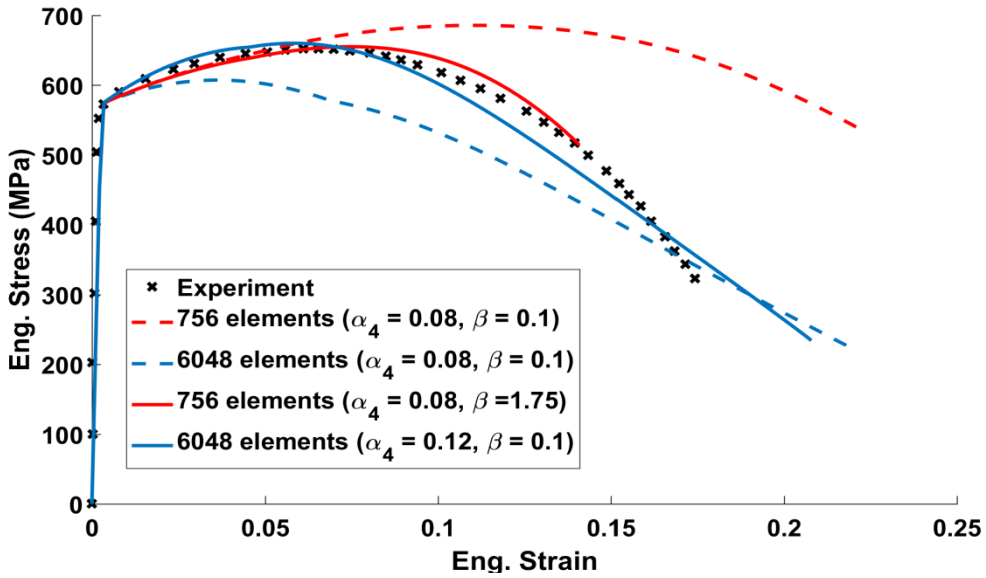

Figure 12: *Mesh sensitivity in damaged model and curve fitting processes by controlling α_4 and β.*

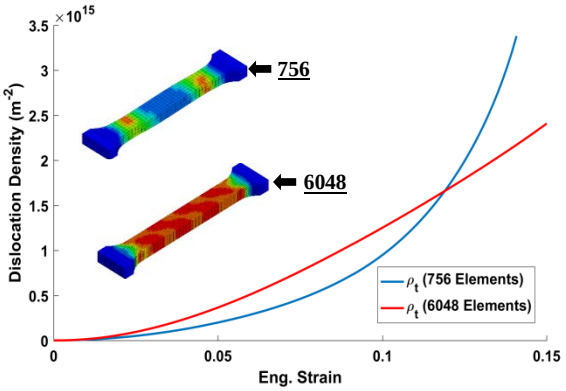

Figure 13: *Comparison between mesh size 756 and 6048 elements for ρ_t.*

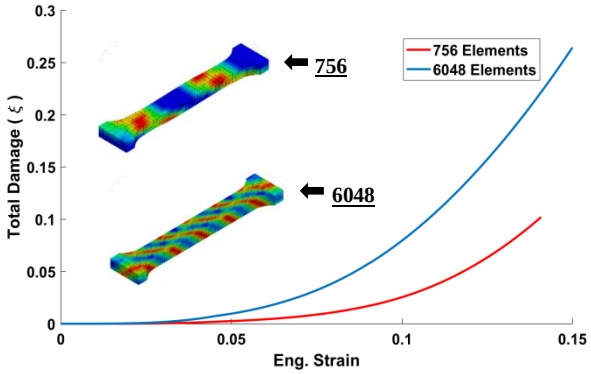

Figure 11: *Comparison between mesh size 756 and 6048 elements for ξ.*

Conclusion

A continuum model of deformation and damage is constructed based on the strain gradient theory to describe the X70 pipelines steel. The model is formulated numerically according to the elastic/viscoplastic framework, and the hardening behavior is described by the accumulation of the densities of the statistically stored dislocations and geometrically necessary stored dislocations. However, the softening behavior, ductile failure, is described by the nucleation and growth of voids according to an isotropic damage model. The model is implemented in a LS-DYNA UMAT subroutine. The model is examined for different strain rates, mesh sizes, and scales. The model shows sensitivity to mesh size when the damage parameter is considered. In addition, the model shows a size effect at a submicron-scale analysis due to gradient effects. The simulation results of the model agree with the experiment results found in the literature.

References

1 S.K. Sharma and S. Maheshwari: *J. Nat. Gas Sci. Eng.*, 2017, vol. 38, pp. 203–17.
2 T. Bellahcene, J. Capelle, M. Aberkane, and Z. Azari: *Appl. Mech. Mater.*, 2011, vol. 146, pp. 213–25.
3 F. Rivalin, A. Pineau, M. Di Fant, and J. Besson: *Eng. Fract. Mech.*, 2001, vol. 68, pp. 329–45.
4 F. Rivalin, J. Besson, A. Pineau, and M. Di Fant: *Eng. Fract. Mech.*, 2000, vol. 68, pp. 347–64.
5 Y. Chen and S. Lambert: *Int. J. Press. Vessel. Pip.*, 2005, vol. 82, pp. 417–26.
6 S.H. Hashemi: *Int. J. Press. Vessel. Pip.*, 2008, vol. 85, pp. 879–84.
7 H.L. Haskel, E. Pauletti, J. de P. Martins, and A.L.M. de Carvalho: *Mater. Res.*, 2014, vol. 17, pp. 1238–50.
8 N.H. Kim, C.S. Oh, Y.J. Kim, K.B. Yoon, and Y.H. Ma: *Int. J. Press. Vessel. Pip.*, 2011, vol. 88, pp. 434–47.
9 Y. Chen and S. Lambert: *Int. J. Fract.*, 2003, vol. 124, pp. 179–99.
10 Y.M. Kim, S.Y. Shin, H. Lee, B. Hwang, S. Lee, and N.J. Kim: *Metall. Mater. Trans. A Phys. Metall. Mater. Sci.*, 2007, vol. 38, pp. 1731–42.
11 L. Zhang, X.G. Li, C.W. Du, and Y.F. Cheng: *J. Mater. Eng. Perform.*, 2009, vol. 18, pp. 319–23.
12 Z.Y. Liu, X.G. Li, C.W. Du, G.L. Zhai, and Y.F. Cheng: *Corros. Sci.*, 2008, vol. 50, pp. 2251–7.
13 M. Paredes, T. Wierzbicki, and P. Zelenak: *Eng. Fract. Mech.*, 2016, vol. 168, pp. 92–111.
14 W. Wang, Y. Shan, and K. Yang: *Mater. Sci. Eng. A*, 2009, vol. 502, pp. 38–44.
15 W. Wang, W. Yan, L. Zhu, P. Hu, Y. Shan, and K. Yang: *Mater. Des.*, 2009, vol. 30, pp. 3436–43.
16 S. Wang, Y. Zhang, and W. Chen: *J. Mater. Sci.*, 2001, vol. 6, pp. 1931–8.
17 L. Zhang, X. gang LI, and C. wei DU: *J. Iron Steel Res. Int.*, 2009, vol. 16, pp. 52–7.
18 X. Zuo and Z. Zhou: *Mater. Res.*, 2015, vol. 18, pp. 36–41.
19 S. de Luna, J. Fernández-Sáez, J.. Pérez-Castellanos, and C. Navarro: *Int. J. Press. Vessel. Pip.*, 2000, vol. 77, pp. 691–6.
20 J.R. Rice and D.M. Tracey: *J. Mech. Phys. Solids*, 1969, vol. 17, pp. 201–17.
21 F. Norton: *McGraw-Hill*.
22 V. Tvergaard and A. Needleman: *Acta Metall.*, 1984, vol. 32, pp. 157–69.
23 W. Ramberg and W.R. Osgood: *Description of Stress Strain Curves by Three Parameters*, Washington DC, 1943.
24 C.K. Oh, Y.J. Kim, J.H. Baek, Y.P. Kim, and W. Kim: *Int. J. Mech. Sci.*, 2007, vol. 49, pp. 1399–412.
25 Y. Li and T. Wierzbicki: *Int. J. Solids Struct.*, 2010, vol. 47, pp. 2316–27.
26 Y. Bai and T. Wierzbicki: *Int. J. Fract.*, 2010, vol. 161, pp. 1–20.
27 D. Hull and D.J. Bacon: *Introduction to Dislocations*, Fourth., Butterworth-Heinemann, Oxford, 2001.
28 A. Pineau, A.A. Benzerga, and T. Pardoen: *Acta Mater.*, 2016, vol. 107, pp. 424–83.
29 M.F. Ashby: *Philos. Mag.*, 1970, vol. 21, pp. 399–424.
30 X. Qiu, Y. Huang, Y. Wei, H. Gao, and K.C. Hwang: *Mech. Mater.*, 2003, vol. 35, pp. 245–58.
31 N.A. Fleck: *Adv. Appl. Mech.*, 1997, vol. 33, pp. 296–362.
32 E.C. Aifantis: *Mech. Mater.*, 2003, vol. 35, pp. 259–80.
33 E.C. Aifantis: *Int. J. Eng. Sci.*, 1992, vol. 30, pp. 1279–99.
34 E.C. Aifantis: *J. Eng. Mater. Technol.*, 1984, vol. 106, p. 326.
35 H.M. Zbib and E.C. Aifantis: *Acta Mech.*, 1992, vol. 92, pp. 209–25.
36 R.H.J. Peerlings: *Mech. Mater.*, 2012, p. 761.
37 J. Lemaitre: *A Course on Damage Mechanics*, 1996.
38 S. Murakami: *Continuum Damage Mechanics*, 2012.
39 J. Besson: *Continuum Models of Ductile Fracture: A Review*, vol. 19, 2010.
40 L.M. Kachanov: *Izv Akad Nauk S S R Otd Tech Nauk*, 1958, vol. 8, pp. 26–31.
41 J. Lemaitre: *J. Eng. Mater. Technol.*, 1985, vol. 107, pp. 83–9.
42 A.L. Gurson: *J. Eng. Mater. Technol.*, 1977, vol. 99, p. 2.
43 G. Rousselier: *Nucl. Eng. Des.*, 1987, vol. 105, pp. 97–111.
44 P. Perzyna: *J. Eng. Mater. Technol.*, 1984, vol. 106, p. 410.
45 Livermore Software Technology Corporation: *LS-DYNA Keyword User'S Manual*, vol. I, 2017.
46 L.E. Malvern: *Introduction to the Mechanics of a Continuous Medium*, Prentice-Hall, Inc., Upper Saddle River, NJ, 1969.
47 A. Needleman: *J. Appl. Mech.*, 1989, vol. 56, pp. 1–9.
48 P. Perzyna: *Mech. Teor. Stos.*, 1963, vol. 1(2), pp. 3–30.
49 G.I. Taylor: *Proc. R. Soc. London. Ser. A, …*, 1934, vol. 145, pp. 362–87.
50 Y. Huang, H. Gao, W.D. Nix, and J.W. Hutchinson: *J. Mech. Phys. Solids*, 2000, vol. 48, pp. 99–128.
51 H. Gao, Y. Huang, W.D. Nix, and J.W. Hutchinson: *J. Mech. Phys. Solids*, 1999, vol. 47, pp. 1239–63.
52 H. Gao and Y. Huang: *Scr. mater.*, 2003, vol. 48, pp. 113–8.
53 J. Pilling and N. Ridley: *Res Mech.*, 1988, vol. 23, pp. 31–63.
54 M.A. Khaleel, H.M. Zbib, and E.A. Nyberg: *Int. J. Plast.*, 2001, vol. 17, pp. 277–96.
55 J.O. Hallquist: *LS-DYNA Theory Manual*, Livermore Software Technology Corporation, Livermore, CA, 2006.

56 ASTM Int.: *Standard Test Methods for Tension Testing of Metallic Materials 1*, 2009.
57 T. Shintani and Y. Murata: *Acta Mater.*, 2011, vol. 59, pp. 4314–22.
58 R. Kishor, L. Sahu, K. Dutta, and A.K. Mondal: *Mater. Sci. Eng. A*, 2014, vol. 598, pp. 299–303.
59 A.A.H. Ameri, N.N. Elewa, M. Ashraf, J.P. Escobedo-Diaz, and P.J. Hazell: in *Characterization of Minerals, Metals, and Materials 2017*, Springer, Cham, 2017, pp. 441–9.